

Article

Petrographical and Geochemical Signatures Linked to Fe/Mn Reduction in Subsurface Marine Sediments from the Hydrate-Bearing Area, Dongsha, the South China Sea

Xi Xiao ^{1,2,3,4,†}, Qian-Zhi Zhou ^{1,†} , Shao-Ying Fu ^{3,4}, Qian-Yong Liang ^{3,4}, Xiang-Po Xu ¹, Yan Li ^{1,*} and Jiang-Hai Wang ^{1,2,*} 

¹ Guangdong Provincial Key Laboratory of Marine Resources and Coastal Engineering, School of Marine Sciences, Sun Yat-Sen University, Guangzhou 510006, China; xiaoxi_629@126.com (X.X.); zhouqzhi@mail2.sysu.edu.cn (Q.-Z.Z.); xuxp35@mail2.sysu.edu.cn (X.-P.X.)

² Southern Marine Science and Engineering Guangdong Laboratory (Zhuhai), Zhuhai 519000, China

³ Guangzhou Marine Geological Survey, Guangzhou 510760, China; fushao@foxmail.com (S.-Y.F.); tomlqy@163.com (Q.-Y.L.)

⁴ Gas Hydrate Engineering Technology Center, China Geological Survey, Guangzhou 510075, China

* Correspondence: liyan255@mail.sysu.edu.cn (Y.L.); wangjhai@mail.sysu.edu.cn (J.-H.W.); Tel.: +86-20-3933-2215 (Y.L.); +86-20-3933-2212 (J.H.W.); Fax: +86-20-8526-1499 (Y.L. & J.H.W.)

† The authors contributed equally to this work.

Received: 17 September 2019; Accepted: 8 October 2019; Published: 11 October 2019



Abstract: Fe and Mn oxides and (oxy)-hydroxides are the most abundant solid-phase electron acceptors in marine sediments, and dissimilatory Fe/Mn reduction usually links with the anaerobic oxidation of methane (AOM) and organic matter oxidation (OMO) in sediments. In this study, we report the results from subsurface marine sediments in the Dongsha hydrate-bearing area in the South China Sea. The petrological and geochemical signatures show that the Fe/Mn reduction mediated by AOM and OMO might occur in sediments above the sulfate-methane transition zone. X-ray diffraction and scanning electron microscopy analyses of sediments indicate that Fe(III)/Mn(IV)-oxides and authigenic carbonate minerals coexisted in the Fe/Mn reduction zone. The lower $\delta^{13}\text{C}$ values of dissolved inorganic carbon, coupled with an evident increase in total inorganic carbon contents and a decrease in Ca^{2+} and Mg^{2+} concentrations indicate the onset of AOM in this zone, and the greater variation of PO_4^{3-} and NH_4^+ concentrations in pore water suggests the higher OMO rates in subsurface sediments. Geochemical and mineralogical analyses suggest that the previously buried Fe(III)/Mn(IV) oxides might be activated and lead to the onset of Fe/Mn reduction induced by AOM and OMO. These findings may extend our understanding of the biogeochemical processes involved in Fe/Mn reduction in continental shelves with abundant methane, organic matter, and terrigenous metal oxides.

Keywords: iron/manganese reduction; anaerobic oxidation of methane; organic matter oxidation; hydrate-bearing area; South China Sea

1. Introduction

Iron (Fe) and manganese (Mn) oxides and (oxy)-hydroxides are the most abundant solid-phase electron acceptors in marine sediments [1]. Following the discovery and confirmation of microorganisms with the capacity to conserve energy from Fe(III) and Mn(IV) reduction in marine sediments, it has been found that dissimilatory microbial metal reduction plays a very important role in early diagenesis [2]. Based on the ‘redox cascade’ in the diagenetic process, organic matter oxidation (OMO) occurs through

a sequence of reduction processes involving oxygen, nitrite, nitrate, high-valence manganese (Mn^{4+}) and iron (Fe^{3+}) oxides, and sulfate above the sulfate-methane transition zone (SMTZ) in sediments [3–6]. Metal reduction, coupled with OMO takes place mostly in suboxic zones [5,7]. In sediments from the Skagerrak, Panama Basin, Black Sea, and the northern Barents Sea, Mn reduction was a dominant process coupled with anaerobic carbon oxidation at a depth of 10 cm in the upper sediments below the free oxygen zone [8–12]. Similarly, Reyes et al. summarized that the bacterial community had been shown to link with the ongoing Fe reduction at the top 30 cm depth in freshwater and marine sediments [13–17].

For the last decade, with the discovery of a new type of anaerobic oxidation of methane (AOM) driven by the reduction of oxidized metal substances in marine sediments [18], metal-driven AOM has been recognized as one of the momentous pathways for oxidizing methane in marine sediments, freshwater, and coastal wetlands [18–22].

Dissimilatory Fe/Mn reduction may dominate AOM in marine sediments with high concentrations of Fe/Mn oxides. However, the microorganisms responsible for this process are largely unknown [12,23]. Unlike other environmentally relevant electron acceptors, metal oxides exist mostly in the form of structural or crystalline minerals, which are insoluble and hard to utilize by microbes [23,24], and the responsible microbes and their biochemical strategies are difficult to pinpoint the locations where dissimilatory Fe/Mn reduction is a predominant pathway in marine environments [17]. Nevertheless, geochemical studies can provide solid evidence to identify the onset of metal reduction in sediments. In 2009, Beal et al. demonstrated that birnessite (MnO_2) and ferrihydrite [$\text{Fe}(\text{OH})_3$] could be used as electron acceptors to oxidize methane in marine methane-seep sediments [18]. Sivan et al. obtained the $\delta^{56}\text{Fe}$ values of iron cations in pore water (−1.66‰ to −2.33‰) [21], which were similar to those of the other sediments with an active dissimilatory bacterial iron reduction [25]. Recently, Fe-rich carbonate chimneys/pipes (mainly composed of aragonite, magnesium-rich calcite, dolomite, ankerite, and siderite) in the northern Okinawa Trough were systematically investigated and might be attributed to the involvement of Fe-driven AOM [26–28]. Field observations revealed that metal-driven AOM generally occurred at sites where other electron acceptors, especially sulfates, were depleted just like those in brackish water estuaries [14] or in methanogenic zones below the SMTZ with abundant Fe/Mn-oxides and dissolved low-valence Fe/Mn cations [20,29–31].

Differently from those observations, our previous study suggested that the Fe/Mn reduction linked with AOM might appear at the depth of 350–490 cm above the SMTZ in the core DH-CL14 from the Dongsha hydrate-bearing area, the South China Sea (SCS), as revealed by the depth-related coupling relation between the abundances of methane-oxidizing bacteria and sulfate-reducing bacteria (SRBs) [32]. A similar case study demonstrated the coupling between AOM/OMO and sulfate/Fe(III) reduction in the zone above the SMTZ at the site of the same research region with high methane flux [33]. Here, we report the detailed petrological and geochemical results from sediment core DH-CL14 and provide evidence for the onset of Fe/Mn reduction coupled with AOM and OMO in subsurface sediments at a depth of several centimeters above the SMTZ. Our new results may help us to further clarify the biogeochemical processes associated with Fe/Mn reduction in continental shelves with abundant methane, organic matter, and terrigenous metal oxides.

2. Materials and Methods

2.1. Study Background

The SCS is one of the largest marginal seas in the western Pacific Ocean. The extensional and strike-slip fault system of the Dongsha area, the northeastern continental slope of the SCS (Figure 1a), provides a favorable condition for the migration of methane fluids and hydrate formation [34]. For several decades, the geological, geochemical, and geophysical studies have revealed a good potential in the resource of natural gas hydrates in the Dongsha area, such as methane-derived carbonates, anomalies of halogens and oxygen isotopes, shallower SMTZ, and bottom-simulating reflectors (BSRs) [35,36]. Previous investigations have reported active methane seep with the methane

gas plume, abundant living seep mussels, and authigenic carbonates in the northeast of the Dongsha area [37,38]. In this study, we measured the geochemical parameters of pore water in four sediment cores from the Dongsha hydrate-bearing area in the SCS. The other three shorter cores with the length of 200–700 cm possessed the similar vertical variations in the functional gene (*apsA*) copies of SRBs and porewater geochemical data with core DH-CL14. Thus, we selected the longest sediment core of DH-CL14 with a length of 738 cm (Figure 1b) for performing the following analyses, as described below. Core DH-CL14 was acquired during China's second gas hydrate drilling expedition (GMGS-2) in the Taixinan Basin, the SCS (Figure 1a). The GMGS-2 was conducted by the Chinese Geological Survey incorporating with Fugro and Geotek from June to September 2013 [39].

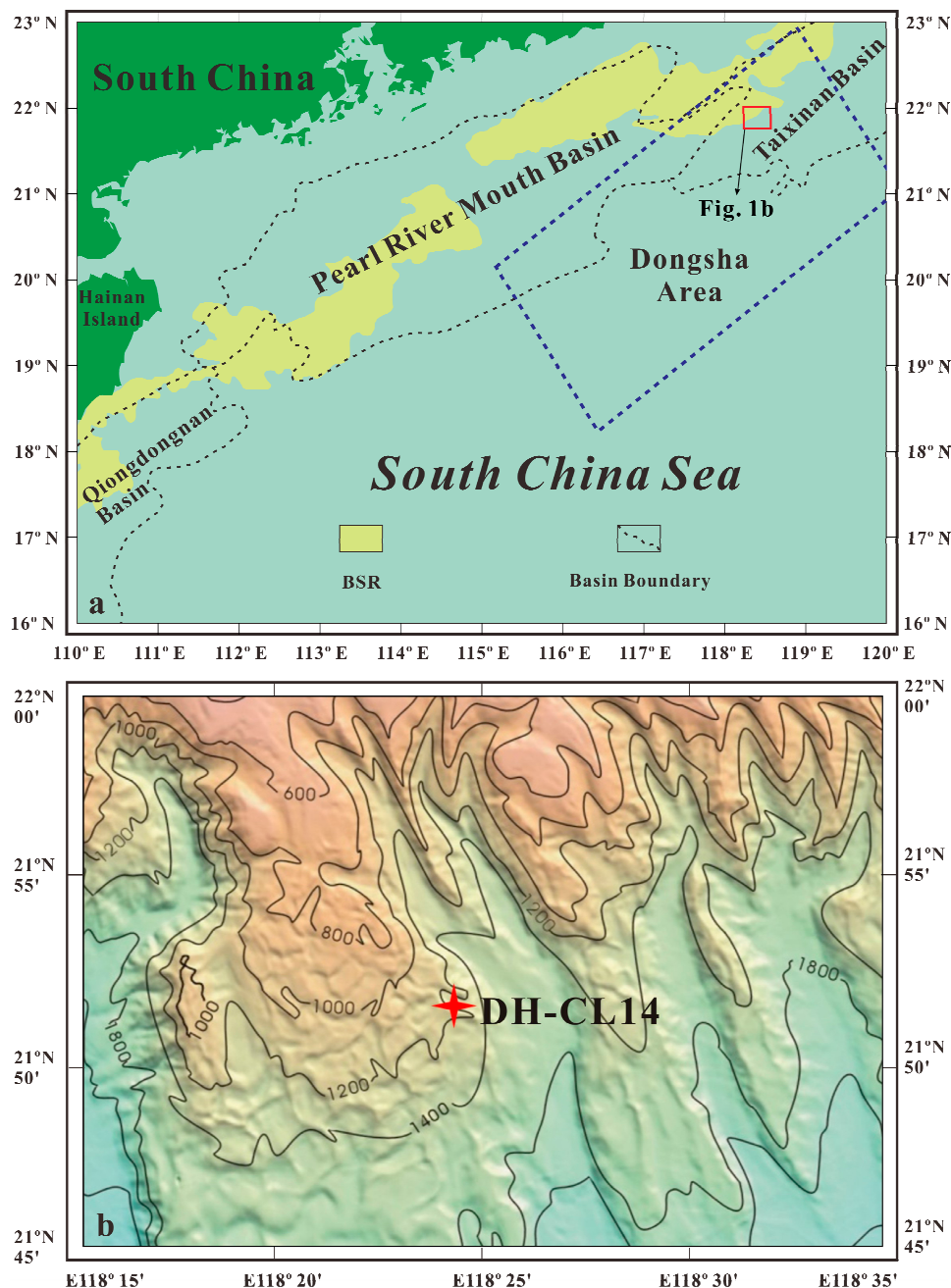


Figure 1. Sketch map illustrating the sampling locality of sediment core DH-CL14 in the Dongsha area, the South China Sea (SCS). (a) Map showing the distribution of main basins in the northern SCS (modified from references [36,40]); (b) Bathymetric map showing the study area and location of the sediment core DH-CL14 (modified from references [32,35]). BSR, bottom-simulating reflectors.

After retrieval, the core was immediately cut into segments on board at the interval of 70 cm from the top down. A total of 22 sediment samples (20 cm thick for each sample) were collected and packed in the zip-lock plastic bags. The air in the bags was pumped out, and the samples were stored at $-20\text{ }^{\circ}\text{C}$. The sampling depths in detail are presented in Table S1.

2.2. Analytical Methods

2.2.1. Analysis of Porewater Geochemistry

Core DH-CL14 was obtained by a gravity piston sampler, and the contents of methane were measured onboard using the headspace equilibration technique by the Agilent 6890N gas chromatograph (Agilent, Palo Alto, CA, USA) equipped with a flame-ionization detector [41]. The pore water was extracted on board at room temperature by a vacuum apparatus [42] from the top 20 cm of a 70 cm thick core section before core freezing. These porewater samples were sealed in numbered plastic bottles and stored at $4\text{ }^{\circ}\text{C}$ for further chemical analyses. Total alkalinity (TA) was analyzed on board by titration with an HCl standard solution [43]. The relative standard deviation (RSD) was less than 2% ($n = 12$). The concentrations of phosphate (PO_4^{3-}) and ammonium (NH_4^+) were photometrically measured on board using a Shimadzu UVmini-1240 spectrophotometer (Shimadzu, Kyoto, Japan) with an analytical error of $\pm 4.0\%$ [44]. About 1.5 mL of each subsample of porewater were added to a 2.5% zinc acetate solution onboard to fix all sulfides as the form of ZnS and stored at $4\text{ }^{\circ}\text{C}$. The concentrations of sulfides were determined in the laboratory using a spectrophotometer [45] by the complexation of the ZnS precipitate in an acidified solution of phenylenediamine and ferric chloride with a detection limit of less than 1 nmol/L. The sulfide standard was validated by titration with thiosulfate to achieve improved accuracy. The contents of sulfate (SO_4^{2-}), calcium (Ca^{2+}), and magnesium (Mg^{2+}) in pore water were determined by using a Metrohm 790 ion chromatograph (IC) (Metrohm, Herisau, Switzerland), with an analytical error of $\pm 1\%$ [46]. The carbon isotope ratios of dissolved inorganic carbon ($\delta^{13}\text{C}_{\text{DIC}}$) in pore water were analyzed by a Delta Plus XP multiflow-isotope ratio mass spectrometer (Finnigan, Bremen, German), with an analytical error of $\pm 0.1\text{‰}$ [42].

2.2.2. Grain Size Analysis

The grain sizes of sediments were analyzed by a Mastersizer 2000 laser particle analyzer (Malvern, Worcestershire, UK) with the measurement range of 0.02–2000 μm , size resolution of 0.01 μm , and measurement error of $<2\%$. Before measuring the grain sizes, these samples were homogenized by ultrasonic vibration, oxidized using 10% H_2O_2 to remove organic matters, and dispersed in a 0.05% solution of sodium hexametaphosphate to separate discrete particles. Grain sizes were classified into three fractions, i.e., sand ($>63\text{ }\mu\text{m}$), silt (4–63 μm), and mud ($<4\text{ }\mu\text{m}$).

2.2.3. Analysis of Total Organic Carbon and Total Inorganic Carbon in Sediments

The contents of total carbon (TC) and total organic carbon (TOC) in sediments were quantitatively measured with a CS230 carbon-sulfur analyzer (Leco, MI, USA) according to an improved method with the optimal pretreatment procedure [47]. The limit of quantification (LOQ) (defined as the mean blank value plus 10 times the standard deviation) was $2.3 \pm 0.3\text{ }\mu\text{g/g}$ TC or TOC per crucible in this study. The total inorganic carbon (TIC) was determined by the difference between TC and TOC.

2.2.4. Major Element Analysis of Sediments

The major element composition of sediments was determined by the PW2424 X-ray fluorescence spectrometry (PANalytical, Almelo, Netherlands) after fusion in lithium nitrate. Lower limits of detection (LLD) for major elements were 0.01%. Spearman's linear correlation among the contents of major elements (wt%) and grain parameters was analyzed by the software IBM SPSS Statistics (Ver. 19, Microsoft, Chicago, IL, USA).

2.2.5. Analysis of Minerals and Sediment Textures

The minerals and sediment textures in core DH-CL14 were analyzed by the system of Quanta 400F FEG field emission environmental scanning electron microscopy (SEM) (FEI, Hillsboro, OR, USA), with the Oxford INCA energy-disperse X-ray spectroscopy (EDS) (Oxford, Bucks, UK), and HKL electron backscattered diffraction (EBSD) facility (HKL, Hobro, Denmark). The analytical conditions are described as below: resolutions for SEM, 2.0 nm (30 kV) and 3.5 nm (3 kV); range of element analysis for EDS: 5B–92U; resolution for EBSD: 0.1 μm (Al, 20 kV); accelerating voltage: 20 kV; and magnification factor: 7–1,000,000. Elemental identification via mapping was performed on the EVO MA 10 SEM (CARL ZEISS, Oberkochen, Germany) with an XFlash 6/30 detector (Bruker, Karlsruhe, Germany). The mineralogical analysis was conducted on powdered sediment samples using a PANalytical Empyrean powder X-ray diffractometer (PANalytical, Almelo, Netherlands) by the monochromatic Cu–K α radiation at 40 kV and 40 mA for identifying mineral phases. The measurement patterns for X-ray powder diffraction (XRD) were recorded between 30° and 80° (2 θ) at the scanning speed of 1 °/min for mainly focusing on iron-manganese minerals. The identification of minerals via XRD was analyzed by the software X'Pert High Score Plus (Ver. 3.0, PANalytical, Almelo, Netherlands), with the International Center for Diffraction Data (ICDD) Database.

3. Results

3.1. Grain Composition of Sediments

The grain composition and its related parameters of sediments, including mean grain size (M_z) and median grain size (M_d), are presented in Table S1. It can be seen from Table S1 that the core is mainly composed of fine-grained silt (56.46–69.82%) and mud (26.16–38.09%) (Table S1; Figure S1). For convenience, the core can be roughly divided into three units (A, B, and C) on the basis of its multiple parameters. It is shown from Table S1 and Figure S1 that the maximum (7.57%) and minimum (6.69%) of its M_z values appear at the depths of 360 cm (the boundary between units A and B) and 500 cm (the border between units B and C), respectively. The M_d values have the same variation trend as that of the M_z values.

3.2. Porewater Geochemistry

The chemical composition of pore water in core DH-CL14 is listed in Table S2 and Figure 2a. It can be seen from Figure 2a that the methane concentrations from units A to B increase gradually from 0.62 mmol/L to 1.34 mmol/L, and then change dramatically from 0.22 mmol/L to the maximum (24.06 mmol/L) in unit C.

Similarly, from units A to B, the sulfate concentrations decrease smoothly from 29 mmol/L (near to the average value in seawater) in the upper sediments to 24 mmol/L at the bottom of unit B. However, the sulfate concentrations decline abruptly down to 11 mmol/L in unit C, and then decrease slightly below the depth of 640 cm (Figure 2a). At the end of this core, the sulfate concentration still maintains at a relatively high level of 10 mmol/L.

The concentrations of dissolved sulfides in units A and B are nearly close to the detection limit, and then rapidly increase to 62 mmol/L in unit C (Figure 2b). Overall, the concentrations of dissolved sulfides exhibit a similar variation trend to those of methane.

The stable carbon isotope composition of dissolved inorganic carbon ($\delta^{13}\text{C}_{\text{DIC}}$) in this core exhibits a relatively monotonic decreasing trend, i.e., from units A to C, the $\delta^{13}\text{C}_{\text{DIC}}$ values decrease gradually from -4.42‰ to -37.31‰ , except the lowest value (-46.20‰) at a depth of 640 cm in unit C (Table S2, Figure 2b).

Both phosphate (PO_4^{3-}) and ammonium (NH_4^+) concentrations in core DH-CL 14 display an obvious increasing trend with depth (Figure 2e,f), ranging from 11.6 $\mu\text{mol/L}$ to 83.7 $\mu\text{mol/L}$ for PO_4^{3-} and 49 $\mu\text{mol/L}$ to 1137 $\mu\text{mol/L}$ for NH_4^+ (Table S2), with the second-highest PO_4^{3-} concentration at a depth of 430 cm.

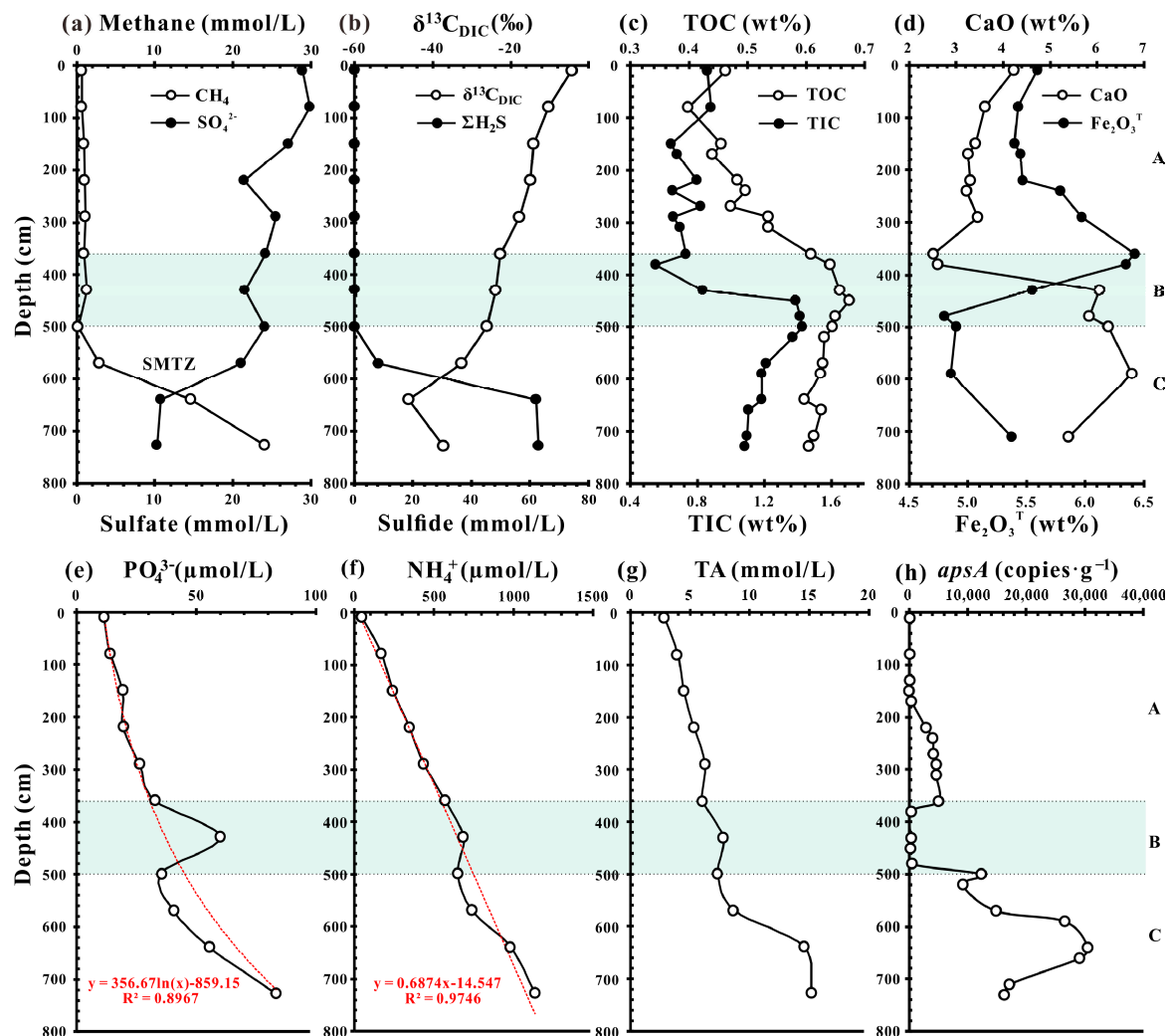


Figure 2. Diagrams showing the variations of geochemical parameters in core DH-CL14. (a) Profiles of methane (CH₄) and sulfate (SO₄²⁻) contents in pore water; (b) Concentrations of dissolved sulfides (ΣH₂S = H₂S + HS⁻ + S²⁻) and stable carbon isotope ratios (δ¹³C) of dissolved inorganic carbon (DIC) in pore water; (c) Contents of total organic carbon (TOC) and total inorganic carbon (TIC) in sediments; and (d) Contents of CaO and Fe₂O₃^T in sediments; Contents of phosphate (PO₄³⁻) (e), ammonium (NH₄⁺) (f), and total alkalinity (TA) (g) in pore water; (h) Copies of *apsA* as the functional gene of SRBs (the data referred from [32]). Units A, B, and C are roughly divided on the basis of diverse geochemical parameters.

Similar to PO₄³⁻ and NH₄⁺, total alkalinity slightly increases from 2.82 mmol/L to 8.68 mmol/L in the upper 570 cm depth but exhibits a great increase up to about 15 mmol/L in unit C (Table S2; Figure 2g).

The concentrations of Ca²⁺ and Mg²⁺ in pore water start to evidently decrease at a depth of 360 cm (9.5 mM and 52 mM, respectively; Table S2), with values much lower than those (Ca²⁺, 10.3 mM; Mg²⁺, 53.2 mM) for the typical seawater [48].

3.3. Contents of TOC and TIC in Sediments

The TOC contents in sediments range from 0.40% to 0.67% with a mean of $0.56 \pm 0.08\%$ (Table S2). It can be seen from Figure 2c that the contents of TOC progressively increase from units A to B from 0.40% to 0.67%, but with a slightly decreasing trend to 0.61% in unit C. The TIC contents suddenly increase from 0.55% to 1.43% in unit B, and then decrease with depth in unit C (Table S2, Figure 2c).

3.4. Composition of Major Elements in Sediments

The contents of major elements in sediments are presented in Table S3. The core is characterized by the high contents of SiO_2 (53.46–61.80%), Al_2O_3 (13.06–16.80%), and $\text{Fe}_2\text{O}_3^{\text{T}}$ (4.80–6.42%), and the relatively low contents of CaO (2.51–6.75%). It can be seen from Figure 2d that the contents of $\text{Fe}_2\text{O}_3^{\text{T}}$ gradually increase from 5.47% to 6.42% at a depth of 220–360 cm, with the highest value at the depth of 360 cm; followed by an abrupt decrease to 4.80% in unit B. Spearman's relation analysis shows that there is a significant positive correlation (significance level, $p < 0.01$) between M_z and Al_2O_3 (correlation coefficient, $\rho = 0.8744$), $\text{Fe}_2\text{O}_3^{\text{T}}$ ($\rho = 0.8304$), or mud ($\rho = 0.7811$) (Table S4). However, there is a significant negative correlation ($p < 0.01$) between the contents of CaO and $\text{Fe}_2\text{O}_3^{\text{T}}$ ($\rho = -0.7525$) (Table S4). The contents of CaO continuously decrease from 4.23% to 2.51% in unit A, while starting to abruptly increase from 360 cm to 590 cm, with a peak of 6.75% at a depth of 590 cm (Figure 2d).

3.5. Mineral Assemblages

The sediments at different depths in core DH-CL14 are mainly composed of detrital minerals (mainly including quartz, feldspar, magnetite, hornblende, biotite, and augite), primordially chemically deposited minerals (ferrihydrite, goethite, lepidocrocite, birnessite, pyrochroite, and manganite), and authigenic minerals (such as calcite, aragonite, dolomite, pyrite, rhodochrosite, and siderite) (Figure S2). Based on the XRD results, Mn-bearing minerals are further identified as birnessite, pyrochroite, manganite, and rhodochrosites while Fe-bearing minerals are recognized as ferrihydrite, goethite, lepidocrocite, magnetite, siderite, and pyrite.

3.6. Sediment Textures

Scanning electron microscopy-Energy Dispersive Spectrometer (SEM-EDS) analysis was performed to observe pyrite aggregates and Fe/Mn oxyhydroxides/ carbonates textures. Various pyrite aggregates occurred in sediments, such as general framboids, specific framboids with radial overgrowths, just like sunflowers in shape, and long pyrite bands (Figure 3). Pyrite framboids in units A, B, and C exhibit secondary overgrowths, and framboidal cores could be clearly distinguished from their overgrowths (Figure 3a,e,g,h). The initial pore space among the framboids was filled by their overgrowth (Figure 3h). Some pyrite bands were converted into aggregates of euhedral crystals (Figure 3c). Subhedral to euhedral pyrite crystals homogeneously distributed in the sediments showing the octahedral shape with a size of 5–45 μm (Figure 3b,d,f). In fact, the sectional shapes of both the pyrite band and sunflower-shaped framboid may configure a three-dimensional pyrite tube just as revealed by the previous report [49]. Several pyrite tubes are found in units A and C. Most of the tubes vary from 200 μm to 600 μm in length and from 85 μm to 140 μm in diameter; they consist of clustered pyrite framboids (Figure 3c,i). Pyrite tubes generally possess their hollow interiors subsequently filled by pyrite. In addition, diverse pyrite aggregates usually occur in foraminiferan chambers (Figure 3a,f).

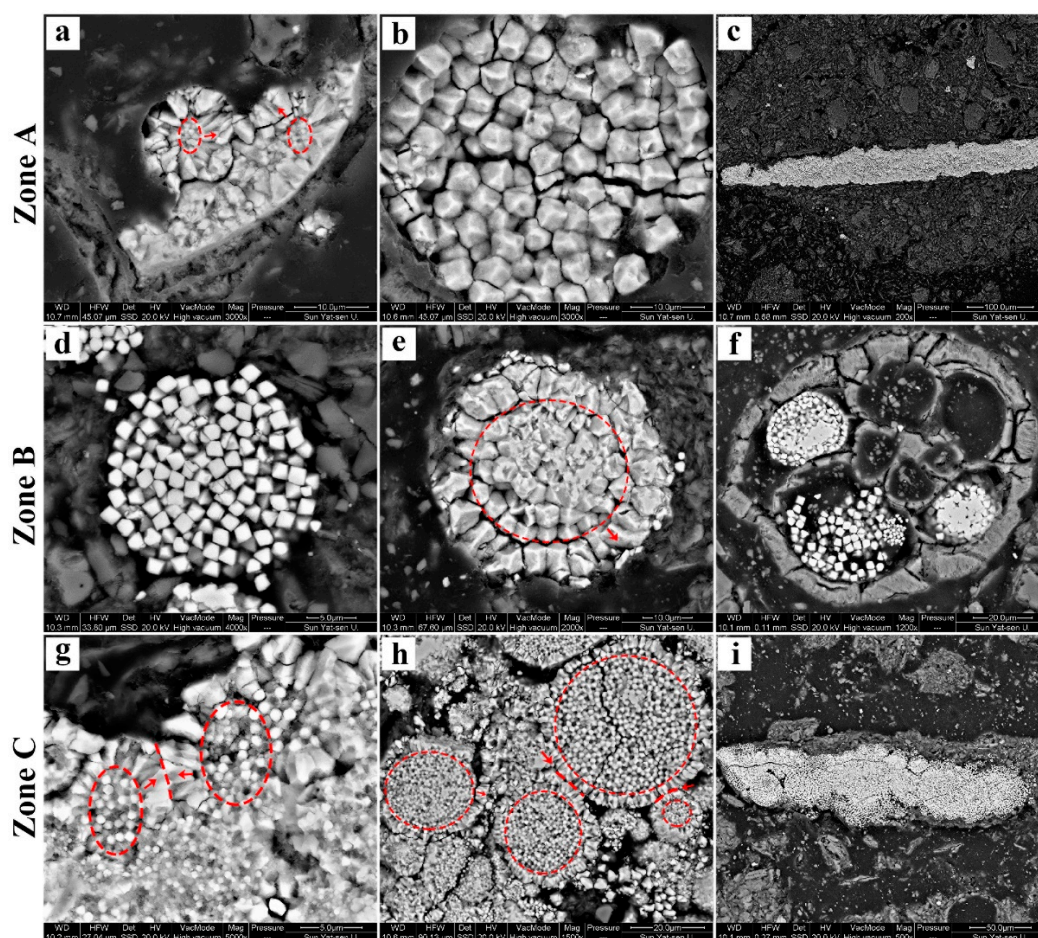


Figure 3. Microscopic morphologies of pyrite aggregates revealed by scanning electron microscopy (SEM) in sediments. Unit A: (a) Sunflower-like pyrite aggregates; (b) Framboid pyrite aggregates; and (c) Longitudinal sections of a pyrite tube. Unit B: (d) Subhedral pyrite aggregates; (e) Euhedral pyrite aggregates with overgrowths; and (f) Subhedral and euhedral pyrite aggregates in foraminiferan chambers. Unit C: (g) and (h) Multiple pyrite framboids with overgrowths; and (i) Longitudinal section of a pyrite tube. Red arrows and ellipses denote the overgrowths of pyrite. The red dashed line indicates the boundary between adjacent sunflower-like pyrite aggregates.

SEM-EDS analysis, combined with elemental identification via mapping, was employed to observe the textures and element distribution of sediments. The analytical results reveal the occurrence of one Fe/Mn microscopic concretion with a size of $285\ \mu\text{m} \times 245\ \mu\text{m}$ at a depth of 380 cm in this core (Figure 4a). The elemental spectra of minerals indicate that the concretion consists of columnar or rhombohedral Mn-oxides and fibrous or botryoidal Fe-oxides (Figure 4 and Figure S3). Combined with the mineral morphologies, columnar aggregates are identified as manganite [$\text{MnO}(\text{OH})$], while rhombohedral polymerides are rhodochrosite (MnCO_3) (Figure 4d). Fibrous and botryoidal minerals with the weaker intensity of electron backscatter diffraction (EBSD) than the other Fe-oxides are lepidocrocite [$\gamma\text{-FeO}(\text{OH})$] and goethite [$\alpha\text{-FeO}(\text{OH})$] (Figure 4a,c,f). Scaly iron minerals with the obviously high peak in element O are siderite (FeCO_3) (Figure 4e and Figure S3d). SEM elemental mapping images exhibit that this concretion is mainly composed of metal elements of Fe (red) and Mn (green) (Figure 4g). Fe-oxides (red) account for about two-thirds of this concretion (Figure 4h,i). Furthermore, Fe- and Mn-oxides with different shapes represent a typical intergrowth (Figure 4g,i).

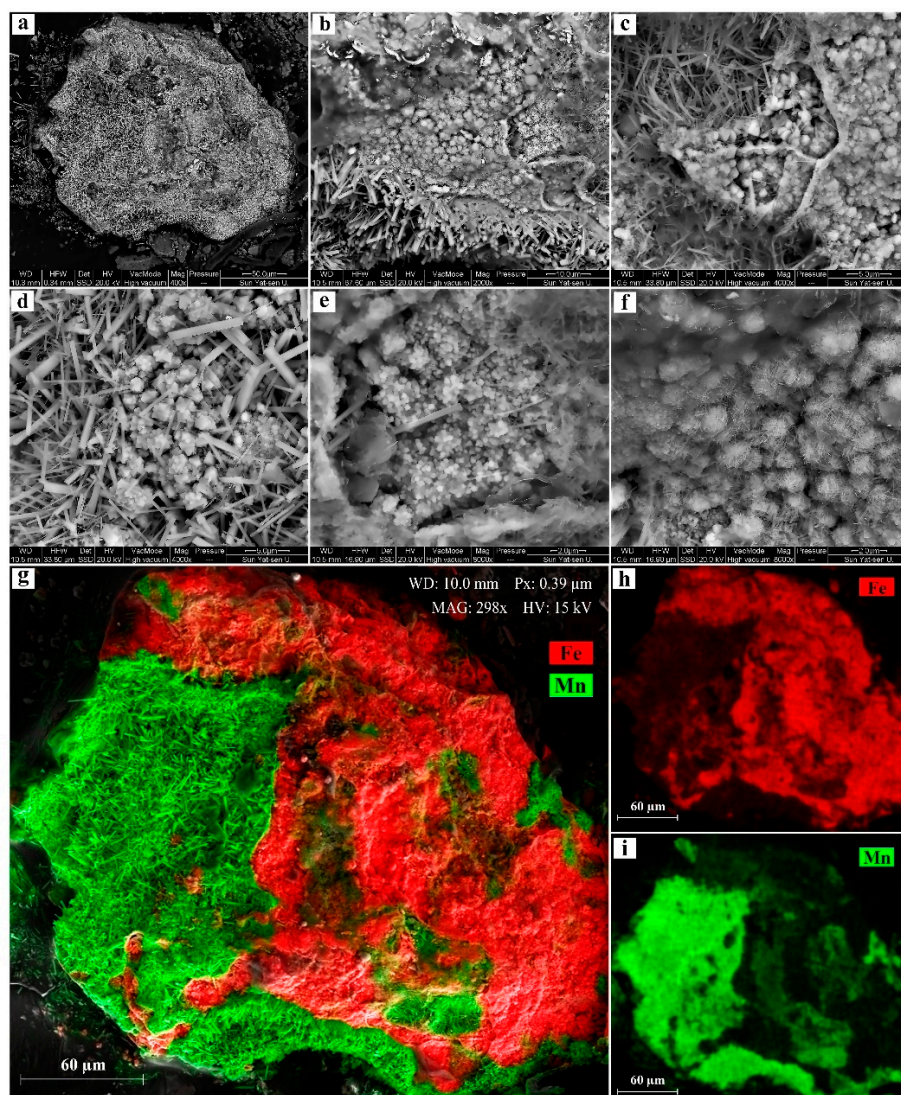


Figure 4. Scanning electron microscope (SEM) photographs showing the microscopic textures and minerals of one Fe/Mn concretion in unit B. (a) Configuration of the Fe/Mn concretion; (b) and (c) Images showing the relationship between the minerals of Mn- and Fe-oxides; (d) Aggregates were composed of columnar manganite and rhombohedral Rhodochrosite; (e) Scaly siderite; (f) Fibrous goethite; (g) SEM elemental mapping for Fe (red) and Mn (green) in the interior of the microscopic concretion; (h) SEM elemental mapping for element Fe in the concretion; and (i) SEM elemental mapping for the element Mn in the concretion.

4. Discussion

4.1. Sulfate Reduction Coupled with AOM in Subsurface Sediments in the Dongsha Area, the SCS

Dongsha is located in the northeastern continental slope of the SCS (Figure 1), where the extensive occurrence of natural gas hydrates and authigenic carbonates indicates high-flux methane seeps [39,50–53]. Numerous studies have also confirmed the onset of AOM in submarine sediments in this region [32,54,55].

In this study, the geochemical profile of the core DH-CL14 exhibits the following signatures of AOM. It could be seen from Figure 2a that the current SMTZ occurs in unit C, where both methane and sulfate are depleted (Figure 2a). Due to the coupling between AOM and sulfate reduction, the concentrations of dissolved sulfide (SH_2S) and CaO display their maximal concentrations while the concentrations of Ca^{2+} and Mg^{2+} decrease rapidly in unit C (Tables S2 and S3, Figure 2b,e).

Meanwhile, abundant authigenic mineral aggregates (Figure 3g,h), especially pyrite tubes (Figure 3i), are accordingly formed in unit C. The $\delta^{13}\text{C}_{\text{DIC}}$ values in pore water continuously decrease until reaching the minimum of -46.2‰ at the depth of 640 cm (Figure 2b), which is consistent with the reported ^{13}C -depleted DIC in the AOM zone [56]. Specific SRBs can utilize methane as their electron donor and co-exist with ANMEs for participating in AOM [57]. Therefore, the quantification of the functional gene *apsA* for SRBs is a rapid detection method for enumerating SRBs in natural environments [26]. As shown in Figure 2h, the highest *apsA* copies ($1.0\text{--}3.1 \times 10^4$ copies/g dry sediments) occurs in unit C (Table S2) [32]. The above evidence may demonstrate the onset of sulfate-driven AOM in unit C [48].

4.2. Petrological and Geochemical Signatures for Fe/Mn Reduction in Unit B

Although the microbially mediated sulfate reduction dominates the pathway with AOM in unit C, it may have not always coupled with AOM in unit B. As revealed in Table S2 and Figure 2h, the relative abundances of SRBs drop dramatically in unit B only with 301–459 copies/g dry sediments, which are one to two orders of magnitude lower than those at the depths of 220–360 cm ($2.9\text{--}5.1 \times 10^3$ copies/g dry sediments) and 500–730 cm ($1.0\text{--}3.1 \times 10^4$ copies/g) [32]. The above results suggest that sulfate reduction may be weakened, whatever is coupled with AOM/OMO, in spite of the maintenance of higher sulfate concentrations. On the other hand, the contents of TIC and CaO abruptly increase in unit B (Figure 2c,d), indicating that the formation of authigenic carbonates may result from the coupling between AOM/OMO and other electron acceptors (i.e., Fe/Mn-oxides) [18,32].

Therefore, sulfate reduction may be limited due to the occurrence of higher Fe contents (4.86–6.42 wt%); and the coupling between Fe(III)/Mn(IV) reduction and AOM/OMO may accordingly be induced in unit B. The above inference is supported by the following petrological and geochemical signatures.

Petrologically, Hein, and Koski pointed out that the ^{13}C -depleted authigenic carbonates associated with rhodochrosite in sediments of the Franciscan Complex (a paleo-analog of the Eel River Basin) recorded the onset of Mn-driven AOM [58]. González et al. reported that the formation of ^{13}C -depleted Fe–Mn carbonate nodules was fueled by the anaerobic oxidation of thermogenic hydrocarbons and organic matter within the channel floor sediments in the Gulf of Cadiz [59]. Sun et al., Peng et al., and Li et al. sequentially found that the carbonate deposits linked to Fe-driven AOM in the northern Okinawa Trough were mainly composed of aragonite, Mg-calcite, dolomite, and siderite [26–28]. In core DH-CL14, the authigenic minerals in unit B mainly include calcite, aragonite, dolomite, siderite, and rhodochrosite (Figures 3, 4 and S2). Particularly, the well-preserved concretion, consisting of rhodochrosite, manganite, siderite, and goethite (Figures 4 and S3) with the specific intergrowth texture (Figure 4g–i) was found in the same environment at a depth of 380 cm. Goethite is usually considered to act as an ideal substrate for Fe-reducing bacteria in natural ecosystems due to its low crystallinity and high specific surface area [26,60–62]. Moreover, siderite has frequently been found in association with calcite in seep environments [63–65]. In this study, the presence of siderite and rhodochrosite indicates that they were formed in an alkaline and non-sulfidic environment with sufficient supplies of Fe-oxides [66,67]. Actually, pyrite tubes are not observed in unit B (Figure 3), and the contents of dissolved sulfides in pore water are as low as 2.0×10^{-6} mmol/L in unit B (Figure 2b), which are propitious to the formation of siderite and rhodochrosite (Figure 4d,e). Obviously, the occurrence of authigenic Fe/Mn microscopic concretions, Fe(III)/Mn(IV)-oxides or -hydroxides (e.g., ferrihydrite, goethite, lepidocrocite, and birnessite), and authigenic minerals (e.g., calcite, Fe-rich dolomite, siderite, and rhodochrosite) indicates that Fe(III)/Mn(IV) reduction may become the dominant process of carbon turnover in unit B [27,59].

Geochemically, core DH-CL14 from the Dongsha area, the SCS has the higher contents of $\text{Fe}_2\text{O}_3^{\text{T}}$ (4.80–6.42%, with a mean of 5.53%) (Table S3, Figure 2d) in comparison with methane-rich sediments in the Nile deep-sea fan, the eastern Mediterranean Sea (mean = 2.05%) [68], iron-enriched carbonates in the Secchia River, the Northern Apennines (mean = 2.48%) [69], and Fe-rich carbonate pipes in the northern Okinawa Trough (4.09–4.63%) [27]. The evident correlation between grain parameters

(particularly mud percentage and Mz) and $Fe_2O_3^T$ contents (Table S4) suggests that iron may result from the terrestrial input of Fe-oxides previously deposited in the continental shelf. The sufficient previously buried Fe(III)-minerals, together with minor Mn(IV)-minerals provided the material sources and created the thermodynamically favorable conditions for metal reduction rather than sulfate reduction for consuming methane or organic matters, and thereby Fe/Mn-rich carbonates precipitated in unit B. Also, it has been proved that the addition of Fe^{3+} can inhibit the reduction of sulfate in sediments [70,71]. Besides, the evident increase in TIC and CaO in unit B (Figure 2c,d) implies the high production of authigenic carbonates and sufficient supply of methane or organic matters as electron donors. Therefore, we infer that the occurrence of excessive high-valence Fe/Mn-oxides (clearly observed in the micro-concretion) in unit B may inhibit microbially-mediated sulfate reduction, and further induce the vertical transition from sulfate reduction in unit C to a high-valence metal reduction in unit B.

4.3. AOM vs. OMO Coupled with Fe/Mn Reduction in Unit B

In anoxic marine sediments, Fe/Mn-oxides are mainly consumed via dissimilatory Fe/Mn reduction, associated with microbially-mediated OMO [72] or AOM. Therefore, how to identify the mechanisms for Fe/Mn reduction is a key issue for evaluating the quantity of methane consumed by metal-driven AOM.

The $\delta^{13}C_{DIC}$ value in pore water is a key parameter for distinguishing AOM from OMO. There are four main sources of DIC in pore water: (1) derived from seawater ($\delta^{13}C_{DIC} \approx 0\text{‰}$); (2) produced during OMO; (3) originated from AOM; (4) from residual DIC after methanogenesis [73]. The sources of inorganic carbon and types of redox reactions could be discriminated against by the $\delta^{13}C_{DIC}$ of pore water. In this work, the $\delta^{13}C_{DIC}$ values range from -22.67‰ (360 cm depth) to -26.12‰ (500 cm depth) in unit B (Table S2; Figure 2b), which are lower than the $\delta^{13}C_{DIC}$ values from the typical marine organic matters in the SCS (-20‰) [74,75]. Therefore, the lower $\delta^{13}C_{DIC}$ values indicate the occurrence of AOM [76], and in turn, lead to the precipitation of carbonates and decrease in the Ca^{2+} and Mg^{2+} concentrations (Table S2, Figure 2c,d).

In this study, the DIC concentrations in this core failed to be detected, but the data of total alkalinity were obtained. In general, the increase in total alkalinity (TA) and concentration of hydrogen sulfide (ΣH_2S) in pore water imply the onset of active sulfate-driven AOM [77]. At the bottom of the core, both TA and ΣH_2S show an evident increase, implying that AOM contributed to sulfate reduction in the SMTZ (Figure 2b,g) [33]. However, not similar to ΣH_2S , TA displays the second peak value at a depth of 430 cm (7.79 mmol/L) (Table S2; Figure 2g), suggesting that AOM was not associated with sulfate, and had a weak effect on TA above the SMTZ.

The profiles of PO_4^{3-} and NH_4^+ are usually utilized for estimating the OMO rate [78] since PO_4^{3-} and NH_4^+ are mainly released in early diagenesis. In contrast to PO_4^{3-} , which can be rapidly consumed in the formation of minerals, NH_4^+ generally does not involve reactions in anoxic marine sediments [79]. The higher concentrations of NH_4^+ in pore water (49–1137 $\mu\text{mol/L}$) indicate higher OMO rates in subsurface sediments (Table S2, Figure 2f) [43]. Nevertheless, the NH_4^+ maximum in core DH-CL 14 is still far lower than that in the Black Sea ($<4.5\text{ mM}$) [80] and the SCS ($<3\text{ mM}$) [81]. The quasi-linear relation of NH_4^+ and logarithmic trend of PO_4^{3-} in pore water with depth display the consistent OMO rates, except that at a depth of 430 cm in unit B (Figure 2e,f). The abrupt rise for PO_4^{3-} in unit B indicates that the reactions between organic matters and Fe/Mn-oxides may be more intense in this sediment layer.

Since OMO is usually homogeneous in a local region, its rate generally depends on the abundances of organic matter and electron acceptors. In the Dongsha area of the SCS, the maximal sedimentation rate after late Pleistocene (41.7 cm/ka) [82] may be comparable to the average in the continental slope [79], but the TOC contents in this core are less than 0.67%. Besides, the evident increase in TIC in unit B (Figure 2c) and the progressive decrease in its $\delta^{13}C_{DIC}$ values with depth (Figure 2b) indicate the contribution of methane. Furthermore, previous studies have proved that the dissimilatory Fe/Mn reduction associated with OMO generally occurs at a depth of several centimeters in the upper surface

sediments [11,12,17]. Therefore, the rapid consumption of excessive high-valence Fe/Mn-oxides in the micro-concretion and evident increase in carbonates imply the onset of the reduction from Fe(III)/Mn(IV) to Fe(II)/Mn(II) induced by AOM and the precipitation of authigenic siderite or rhodochrosite in sediments (Figure 4d,e).

4.4. Probable Biogeochemical Processes for Fe/Mn Reduction in the High-Flux Methane Emission Region

The new petrological and geochemical data, as well as the *apsA* abundances, suggest that Fe/Mn reduction occurred at a depth of several centimeters above the SMTZ and might couple with AOM and/or OMO in the hydrate-bearing region with abundant Fe/Mn-oxides, as described as follows.

Previous studies have shown that metal-driven AOM is widely distributed in the marine sediments with the high input of metal oxides and high-flux methane seeps [29,30,83]. In this case, the study area is located in the northeastern unstable continental slope of the SCS [84] (Figure 1), and the sediments with abundant Fe/Mn-oxides from the shelf of the SCS might be integrally transported into the Dongsha area due to the structural or gravity instability. The previously deposited Fe/Mn-oxides, in particular, goethite, ferrihydrite, and birnessite with large specific surface areas [28,60,61,85], would spontaneously trigger the onset of AOM in the sediments with high-flux methane seeps. Obviously, the Fe/Mn source, in this case, evidently differs from those previously reported in the northern Okinawa Trough (i.e., Fe³⁺ derived from deep-source fluids at methane seeps) [26–28].

Abundant high-valence metal-oxides are widely distributed in various environments, in which AOM decouples with sulfate reduction, but couples with these metal-oxides [83,86]. In a recent co-culture experiment of ferrihydrite reduction and methane oxidation, ferrihydrite was reduced, and ferrous minerals were formed [87]. In submarine sediments, Fe/Mn-oxides such as ferrihydrite and birnessite are important and ubiquitous geosorbents, which have large specific surface areas of more than 200 m²/g [85,88,89] and 63–300 m²/g, respectively [90,91]. In addition, the similar biogeochemical processes of Fe and Mn reduction are found in the hydrocarbon-derived Fe-rich nodules from the Dongsha area and carbonate chimneys from the Gulf of Cadiz [34,92,93]. The input of high-valence Fe-oxides derived from terrigenous sediments in the continental shelf of the Gulf of Cadiz was proved to support the formation of siderite-rhodochrosite nodules from goethite-Mn oxides nodules [59]. Therefore, the sufficient Fe/Mn-oxides may react with methane derived from the deep hydrate-bearing layers.

Meanwhile, the above-mentioned scenario on AOM in core DH-CL14 reveals a specific coexistence between metal- and sulfate-driven AOM in unit B, despite the maintenance of the higher concentrations of sulfate in this unit. Fe(III) in solid Fe-oxides can be activated via microbial mediation [33]. Iron-reducing bacteria, which obtain Fe(III) through the siderophore uptake mechanism, can cooperate with ANMEs to consume Fe(III) and methane, and accordingly, Fe(II) and bicarbonates are formed in Fe-driven AOM in association with the migration of Fe and its accompanying elements [24]. Spontaneously, some sulfides, as the products of sulfate-driven AOM/OMO, react with the byproducts [Fe(II)] of Fe-driven AOM to form sulfide minerals (e.g., pyrite) in this unit (Figure 3d,f). The excessive Fe(II) results in the absence of dissolved sulfide in pore water (Figure 2b) and the occurrence of siderite (Figure 4e). The reducing capacity of hydrocarbons and the role of hydrocarbon-rich fluids as a metal-transporting agent were proved in hydrocarbon escape structures, such as mud volcanoes, related expelled waters, sediments, and authigenic mineralization [59,94,95]. This hydrocarbon flow promoted the migration of fluids with methane, metallic ions, and their complexes in sediments, commonly together with microbial mediation like SRBs [34,59].

In summary, this study provides a good case on the potential methane sink linked with metal-driven AOM in the hydrate-bearing area with abundant methane and terrigenous metal oxides in the northeastern continental slope of the SCS. Although metal-driven AOM probably occurs in the nitrite-, nitrate-, and sulfate-depleted and metal-rich natural environments, its significance still remains unclear at the global scale [18]. Therefore, it is necessary to further clarify the contribution of metal-driven

AOM to the methane sink. If the metal reduction is ignored, its importance will be undervalued, especially in continental shelves with abundant metal oxides [82,96].

5. Conclusions

The petrographical and geochemical signatures indicate the coexistence between metal-driven AOM and OMO at a depth of 380–500 cm above the SMTZ in the sediment core from the Dongsha hydrate-bearing area, the SCS. The profiles of the methane and sulfate concentrations in pore water suggest that the current SMTZ depth in this core is around 600 cm. Above the SMTZ, high-valence Fe/Mn-oxides (e.g., ferrihydrite and birnessite), together with the reaction products (e.g., siderite and rhodochrosite) are firstly discovered in the Fe/Mn microscopic concretions with the intergrowth texture. The lower $\delta^{13}\text{C}_{\text{DIC}}$ values (−22.67‰ to −26.12‰), the increase in TIC, and decrease in Ca^{2+} and Mg^{2+} indicate the onset of AOM in unit B; and the increase in PO_4^{3-} and NH_4^+ in pore water suggests the occurrence of OMO. Based on these findings, Fe/Mn reduction may occur in subsurface sediments at a depth of several centimeters above the SMTZ, which may be mutually mediated by AOM and OMO. Accordingly, a novel probable mechanism has been proposed to expound the complicated biogeochemical processes involved in Fe/Mn reduction in the hydrate-bearing area with abundant methane, organic matter, and terrigenous metal oxides.

Supplementary Materials: The following are available online at <http://www.mdpi.com/2075-163X/9/10/624/s1>. Figure S1: Variations of (a) grain compositions, (b) mean grain size (M_z), and (c) median grain size (M_d) for core DH-CL14; Figure S2: X-ray diffraction patterns of sediment samples at depths of 10 cm (a), 270 cm (b), 380 cm (c), and 730 cm (d) in core DH-CL14, respectively; and Figure S3: Energy dispersive spectroscopy (EDS) analysis of a Fe/Mn microscopic concretion from core DH-CL14; Table S1: Grain composition and parameters of core DH-CL14; Table S2: Geochemical parameters in core DH-CL14; Table S3: Contents of major elements (wt%) in core DH-CL14; Table S4: Spearman's correlation coefficients among the contents of major elements (wt%) and grain parameters in core DH-CL14.

Author Contributions: Conceptualization—J.-H.W. and Y.L.; Methodology—Q.-Z.Z., X.X. and X.-P.X. Analysis—X.X. and X.-P.X.; Resources—S.-Y.F. and Q.-Y.L.; Writing—Original Draft Preparation—X.X. and Q.-Z.Z.; Writing—Review & Editing—J.-H.W. and Y.L.; Funding Acquisition—J.-H.W. and Y.L.

Funding: This work was mutually supported by the National Natural Science Foundation of China (No. 41703043), Guangzhou Marine Geological Survey (No. DD20160214), and Guangzhou Science and Technology (No. 201909010002).

Conflicts of Interest: The authors declare that they have no conflict of interest. The funding sponsors had no role in the design of the study; in the collection, analyses, or interpretation of data; in the writing of the manuscript; or in the decision to publish the results.

References

1. Thamdrup, B. Bacterial manganese and iron reduction in aquatic sediments. *Adv. Microbial. Ecol.* **2000**, *16*, 41–84. [CrossRef]
2. Lovley, D.R. Dissimilatory Fe(III) and Mn(IV) reduction. *Adv. Microb. Physiol.* **2004**, *49*, 219–286. [CrossRef] [PubMed]
3. Emerson, S.; Hedges, J. Sediment diagenesis and benthic flux. *Treatise Geochem.* **2003**, *6*, 293–319. [CrossRef]
4. Canfield, D.E. Sulfate reduction in deep-sea sediments. *Am. J. Sci.* **1991**, *291*, 177–188. [CrossRef] [PubMed]
5. Froelich, P.N.; Klinkhammer, G.P.; Bender, M.L.; Luedtke, N.A.; Heath, G.R.; Cullen, D.; Dauphin, P.; Hammond, D.; Hartman, B.; Maynard, V. Early oxidation of organic matter in pelagic sediments of the eastern equatorial atlantic: Suboxic diagenesis. *Geochim. Cosmochim. Acta* **1979**, *43*, 1075–1090. [CrossRef]
6. Liang, L.; Wang, Y.; Sivan, O.; Wang, F. Metal-dependent anaerobic methane oxidation in marine sediment: Insights from marine settings and other systems. *Sci. China Life Sci.* **2019**, 1–9. [CrossRef]
7. Jørgensen, B.B.; Kasten, S. Sulfur cycling and methane oxidation. In *Marine Geochemistry*; Springer: Berlin, Germany, 2006; pp. 271–309.
8. Canfield, D.E.; Thamdrup, B.; Hansen, J.W. The anaerobic degradation of organic matter in danish coastal sediments: Iron reduction, manganese reduction, and sulfate reduction. *Geochim. Cosmochim. Acta* **1993**, *57*, 3867–3883. [CrossRef]

9. Nickel, M.; Vandieken, V.; Bruechert, V.; Jørgensen, B.B. Microbial Mn(IV) and Fe(III) reduction in northern Barents Sea sediments under different conditions of ice cover and organic carbon deposition. *Deep Sea Res. Part II* **2008**, *55*, 2390–2398. [[CrossRef](#)]
10. Thamdrup, B.; Dalsgaard, T. The fate of ammonium in anoxic manganese oxide-rich marine sediment. *Geochim. Cosmochim. Acta* **2000**, *64*, 4157–4164. [[CrossRef](#)]
11. Vandieken, V.; Nickel, M.; Jørgensen, B.B. Carbon mineralization in Arctic sediments northeast of Svalbard: Mn(IV) and Fe(III) reduction as principal anaerobic respiratory pathways. *Mar. Ecol. Prog. Ser.* **2006**, *322*, 15–27. [[CrossRef](#)]
12. Vandieken, V.; Pester, M.; Finke, N.; Hyun, J.H.; Friedrich, M.W.; Loy, A.; Thamdrup, B. Three manganese oxide-rich marine sediments harbor similar communities of acetate-oxidizing manganese-reducing bacteria. *ISME J.* **2012**, *6*, 2078. [[CrossRef](#)] [[PubMed](#)]
13. Edlund, A.; Jansson, J.K. Changes in active bacterial communities before and after dredging of highly polluted Baltic Sea sediments. *Appl. Environ. Microbiol.* **2006**, *72*, 6800–6807. [[CrossRef](#)] [[PubMed](#)]
14. Lin, B.; Hyacinthe, C.; Bonneville, S. 10.1128/AEM.00971-06 Phylogenetic and physiological diversity of dissimilatory ferric iron reducers in sediments of the polluted Scheldt estuary, Northwest Europe. *Environ. Microbiol.* **2007**, *9*, 1956–1968. [[CrossRef](#)] [[PubMed](#)]
15. Powell, S.M.; Bowman, J.P.; Snape, I.; Stark, J.S. Microbial community variation in pristine and polluted nearshore Antarctic sediments. *FEMS Microbiol. Ecol.* **2003**, *45*, 135–145. [[CrossRef](#)]
16. Sinkko, H.; Lukkari, K.; Jama, A.S.; Sihvonen, L.M.; Sivonen, K.; Leivuori, M.; Lyra, C. Phosphorus chemistry and bacterial community composition interact in brackish sediments receiving agricultural discharges. *PLoS ONE* **2011**, *6*, e21555. [[CrossRef](#)] [[PubMed](#)]
17. Reyes, C.; Dellwig, O.; Dähnke, K.; Gehre, M.; Noriega-Ortega, B.E.; Böttcher, M.E.; Meister, P.; Friedrich, M.W. Bacterial communities potentially involved in iron-cycling in Baltic Sea and North Sea sediments revealed by pyrosequencing. *FEMS Microbiol. Ecol.* **2016**, *92*, fiw054. [[CrossRef](#)]
18. Beal, E.J.; House, C.H.; Orphan, V.J. Manganese- and iron-dependent marine methane oxidation. *Science* **2009**, *325*, 184–187. [[CrossRef](#)]
19. Cai, C.; Leu, A.O.; Xie, G.J.; Guo, J.; Hu, S. A methanotrophic archaeon couples anaerobic oxidation of methane to Fe(III) reduction. *ISME J.* **2018**, *12*, 1929–1939. [[CrossRef](#)]
20. Egger, M.; Rasigraf, O.; Sapart, C.J.; Jilbert, T.; Jetten, M.S.; Röckmann, T.; Van der Veen, C.; Banda, N.; Kartal, B.; Ettwig, K.F. Iron-mediated anaerobic oxidation of methane in brackish coastal sediments. *Environ. Sci. Technol.* **2014**, *49*, 277–283. [[CrossRef](#)]
21. Sivan, O.; Adler, M.; Pearson, A.; Gelman, F.; Bar-Or, I.; John, S.G.; Eckert, W. Geochemical evidence for iron-mediated anaerobic oxidation of methane. *Limnol. Oceanogr.* **2011**, *56*, 1536–1544. [[CrossRef](#)]
22. Weber, H.S.; Habicht, K.S.; Thamdrup, B. Anaerobic methanotrophic archaea of the ANME-2d cluster are active in a low-sulfate, iron-rich freshwater sediment. *Front. Microbiol.* **2017**, *8*, 619–631. [[CrossRef](#)] [[PubMed](#)]
23. Oni, O.E.; Friedrich, M.W. Metal oxide reduction linked to anaerobic methane oxidation. *Trends Microbiol.* **2017**, *25*, 88–90. [[CrossRef](#)] [[PubMed](#)]
24. Canfield, D.E. Reactive iron in marine sediments. *Geochim. Cosmochim. Acta* **1989**, *53*, 619–632. [[CrossRef](#)]
25. Severmann, S.; Johnson, C.M.; Beard, B.L.; Mcmanus, J. The effect of early diagenesis on the Fe isotope compositions of porewaters and authigenic minerals in continental margin sediments. *Geochim. Cosmochim. Acta* **2006**, *70*, 2006–2022. [[CrossRef](#)]
26. Li, J.; Peng, X.; Bai, S.; Chen, Z.; Van Nostrand, J.D. Biogeochemical processes controlling authigenic carbonate formation within the sediment column from the Okinawa Trough. *Geochim. Cosmochim. Acta* **2018**, *222*, 363–382. [[CrossRef](#)]
27. Peng, X.; Guo, Z.; Chen, S.; Sun, Z.; Xu, H.; Ta, K.; Zhang, J.; Zhang, L.; Li, J.; Du, M. Formation of carbonate pipes in the northern Okinawa Trough linked to strong sulfate exhaustion and iron supply. *Geochim. Cosmochim. Acta* **2017**, *205*, 1–13. [[CrossRef](#)]
28. Sun, Z.; Wei, H.; Zhang, X.; Shang, L.; Yin, X.; Sun, Y.; Xu, L.; Huang, W.; Zhang, X. A unique Fe-rich carbonate chimney associated with cold seeps in the Northern Okinawa Trough, East China Sea. *Deep Sea Res. Part I* **2015**, *95*, 37–53. [[CrossRef](#)]
29. Oni, O.; Miyatake, T.; Kasten, S.; Richter-Heitmann, T.; Fischer, D.; Wagenknecht, L.; Kulkarni, A.; Blumers, M.; Shylin, S.I.; Ksenofontov, V. Distinct microbial populations are tightly linked to the profile of dissolved iron in the methanogenic sediments of the Helgoland mud area, North Sea. *Front. Microbiol.* **2015**, *6*, 365–379. [[CrossRef](#)]

30. Riedinger, N.; Formolo, M.J.; Lyons, T.W.; Henkel, S.; Beck, A.; Kasten, S. An inorganic geochemical argument for coupled anaerobic oxidation of methane and iron reduction in marine sediments. *Geobiology* **2014**, *12*, 172–181. [[CrossRef](#)] [[PubMed](#)]
31. Vigderovich, H.; Liang, L.; Herut, B.; Wang, F.; Wurgaft, E.; Rubin-Blum, M.; Sivan, O. Evidence for microbial iron reduction in the methanogenic sediments of the oligotrophic SE Mediterranean continental shelf. *Biogeosci. Discuss* **2019**, *16*, 1–25. [[CrossRef](#)]
32. Xu, X.M.; Fu, S.Y.; Zhu, Q.; Xiao, X.; Yuan, J.P.; Peng, J.; Wu, C.F.; Wang, J.H. Depth-related coupling relation between methane-oxidizing bacteria (MOBs) and sulfate-reducing bacteria (SRBs) in a marine sediment core from the Dongsha region, the South China Sea. *Appl. Microbiol. Biotechnol.* **2014**, *98*, 10223–10230. [[CrossRef](#)] [[PubMed](#)]
33. Li, J.; Li, L.; Bai, S.; Ta, K.; Xu, H.; Chen, S.; Pan, J.; Li, M.; Du, M.; Peng, X. New insight into the biogeochemical cycling of methane, S and Fe above the Sulfate-Methane Transition Zone in methane hydrate-bearing sediments: A case study in the Dongsha area, South China Sea. *Deep Sea Res. Part I* **2019**, *145*, 97–108. [[CrossRef](#)]
34. Zhong, Y.; Chen, Z.; González, F.J.; Hein, J.R.; Zheng, X.; Li, G.; Luo, Y.; Mo, A.; Tian, Y.; Wang, S. Composition and genesis of ferromanganese deposits from the northern South China Sea. *J. Asian Earth Sci.* **2017**, *138*, 110–128. [[CrossRef](#)]
35. Huang, Y.X.; Suess, E.; Wu, N.Y. *Methane and Gas Hydrate Geology of the Northern South China Sea: Sino-German Cooperative So-177 Cruise Report*; Geological Publishing House: Beijing, China, 2008; p. 48.
36. Li, L.; Lei, X.; Zhang, X.; Sha, Z. Gas hydrate and associated free gas in the dongsha area of northern South China Sea. *Mar. Petrol. Geol.* **2013**, *39*, 92–101. [[CrossRef](#)]
37. Feng, D.; Chen, D. Authigenic carbonates from an active cold seep of the northern South China Sea: New insights into fluid sources and past seepage activity. *Deep Sea Res. Part II* **2015**, *122*, 74–83. [[CrossRef](#)]
38. Feng, D.; Cheng, M.; Kiel, S.; Qiu, J.W.; Yang, Q.; Zhou, H.; Peng, Y.B.; Chen, D. Using *Bathymodiolus* tissue stable carbon, nitrogen and sulfur isotopes to infer biogeochemical process at a cold seep in the South China Sea. *Deep Sea Res. Part I* **2015**, *104*, 52–59. [[CrossRef](#)]
39. Zhang, G.; Liang, J.; Lu, J.A.; Yang, S.; Zhang, M.; Holland, M.; Schultheiss, P.; Su, X.; Sha, Z.; Xu, H.; et al. Geological features, controlling factors and potential prospects of the gas hydrate occurrence in the east part of the Pearl River Mouth Basin, South China Sea. *Mar. Petrol. Geol.* **2015**, *67*, 356–367. [[CrossRef](#)]
40. Gong, J.; Sun, X.; Xu, L.; Lu, H. Contribution of thermogenic organic matter to the formation of biogenic gas hydrate: Evidence from geochemical and microbial characteristics of hydrate-containing sediments in the Taixinan Basin, South China Sea. *Mar. Petrol. Geol.* **2017**, *80*, 432–449. [[CrossRef](#)]
41. Wu, L.; Yang, S.; Liang, J.; Su, X.; Fu, S.; Sha, Z.; Yang, T. Variations of pore water sulfate gradients in sediments as indicator for underlying gas hydrate in Shenhu Area, the South China Sea. *Sci. China Earth Sci.* **2013**, *56*, 530–540. [[CrossRef](#)]
42. Yang, T.; Jiang, S.Y.; Yang, J.H.; Lu, G.; Wu, N.Y.; Liu, J.; Chen, D.H. Dissolved inorganic carbon (DIC) and its carbon isotopic composition in sediment pore waters from the Shenhu area, northern South China Sea. *J. Oceanogr.* **2008**, *64*, 303–310. [[CrossRef](#)]
43. Cheng, S.H.; Li, Q. A determination method for the alkalinity of pore-water in marine sediment. *Chem. Anal. Meterage* **2012**, *21*, 34–36, (In Chinese with English Abstract). [[CrossRef](#)]
44. Wu, L.S.; Yang, S.X.; Liang, J.Q.; Su, X.; Yang, T.; Zhang, X.; Cheng, S.H.; Lu, H.F. Geochemical characteristics of sediments at site HQ-48PC in Qiongdongnan Area, the north of the South China Sea, and their implication for gas hydrates. *Geoscience* **2010**, *24*, 534–544, (In Chinese with English abstract). [[CrossRef](#)]
45. Cline, J.D. Spectrophotometric determination of hydrogen sulfide in natural waters. *Limnol. Oceanogr.* **1969**, *14*, 454–458. [[CrossRef](#)]
46. Ge, L.; Yang, T.; Jiang, S.Y.; Yang, J.H. Ion chromatogram method for analyzing anions and cations in pore water from marine sediments. *Mar. Geol. Quart. Geol.* **2006**, *26*, 125–130, (In Chinese with English Abstract).
47. Xu, X.M.; Zhu, Q.; Zhou, Q.Z.; Liu, J.Z.; Yuan, J.P.; Wang, J.H. An improved method for quantitatively measuring the sequences of total organic carbon and black carbon in marine sediment cores. *J. Oceanol. Limnol.* **2018**, *36*, 105–113. [[CrossRef](#)]
48. Chen, Y.F.; Ussler, W.I.; Hafliðason, H.; Lepland, A.; Rise, L.; Hovland, M.; Hjelstuen, B.O. Sources of methane inferred from pore-water $\delta^{13}\text{C}$ of dissolved inorganic carbon in Pockmark G11, offshore Mid-Norway. *Chem. Geol.* **2010**, *275*, 127–138. [[CrossRef](#)]

49. Lin, Z.; Sun, X.; Strauss, H.; Lu, Y.; Gong, J.; Xu, L.; Lu, H.; Teichert, B.M.A.; Peckmann, J. Multiple sulfur isotope constraints on sulfate-driven anaerobic oxidation of methane: Evidence from authigenic pyrite in seepage areas of the South China Sea. *Geochim. Cosmochim. Acta*. **2017**, *211*, 153–173. [\[CrossRef\]](#)
50. Sha, Z.; Liang, J.; Zhang, G.; Yang, S.; Lu, J.; Zhang, Z.; McConnell, D.R.; Humphrey, G. A seepage gas hydrate system in northern South China Sea: Seismic and well log interpretations. *Mar. Geol.* **2015**, *366*, 69–78. [\[CrossRef\]](#)
51. Chen, F.; Hu, Y.; Feng, D.; Zhang, X.; Cheng, S.; Cao, J.; Lu, H.; Chen, D. Evidence of intense methane seepages from molybdenum enrichments in gas hydrate-bearing sediments of the northern South China Sea. *Chem. Geol.* **2016**, *443*, 173–181. [\[CrossRef\]](#)
52. Lin, Q.; Wang, J.; Algeo, T.J.; Su, P.; Hu, G. Formation mechanism of authigenic gypsum in marine methane hydrate settings: Evidence from the northern South China Sea. *Deep Sea Res. Part I* **2016**, *115*, 210–220. [\[CrossRef\]](#)
53. Hu, Y.; Chen, L.; Feng, D.; Liang, Q.; Xia, Z.; Chen, D. Geochemical record of methane seepage in authigenic carbonates and surrounding host sediments: A case study from the South China Sea. *J. Asian Earth Sci.* **2017**, *138*, 51–61. [\[CrossRef\]](#)
54. Ge, L.; Jiang, S.Y.; Blumenberg, M.; Reitner, J. Lipid biomarkers and their specific carbon isotopic compositions of cold seep carbonates from the South China Sea. *Mar. Petrol. Geol.* **2015**, *66*, 501–510. [\[CrossRef\]](#)
55. Hu, Y.; Luo, M.; Chen, L.; Liang, Q.; Feng, D.; Tao, J.; Yang, S.; Chen, D. Methane source linked to gas hydrate system at hydrate drilling areas of the South China Sea: Porewater geochemistry and numerical model constraints. *J. Asian Earth Sci.* **2018**, *168*, 87–95. [\[CrossRef\]](#)
56. Ussler, W.; Paull, C.K. Rates of anaerobic oxidation of methane and authigenic carbonate mineralization in methane-rich deep-sea sediments inferred from models and geochemical profiles. *Earth Planet. Sci. Lett.* **2008**, *266*, 271–287. [\[CrossRef\]](#)
57. Boetius, A.; Ravensschlag, K.; Schubert, C.J.; Rickert, D.; Widdel, F.; Gieseke, A.; Amann, R.; Jørgensen, B.B.; Witte, U.; Pfannkuche, O. A marine microbial consortium apparently mediating anaerobic oxidation of methane. *Nature* **2000**, *407*, 623–626. [\[CrossRef\]](#) [\[PubMed\]](#)
58. Hein, J.R.; Koski, R.A. Bacterially mediated diagenetic origin for chert-hosted manganese deposits in the Franciscan Complex, California Coast Ranges. *Geology* **1987**, *15*, 722–726. [\[CrossRef\]](#)
59. González, F.J.; Somoza, L.; León, R.; Medialdea, T.; de Torres, T.; Ortiz, J.E.; Lunar, R.; Martínez-Frías, J.; Merinero, R. Ferromanganese nodules and micro-hardgrounds associated with the Cadiz Contourite Channel (NE Atlantic): Palaeoenvironmental records of fluid venting and bottom currents. *Chem. Geol.* **2012**, *310*, 56–78. [\[CrossRef\]](#)
60. Langley, S.; Igric, P.; Takahashi, Y.; Sakai, Y.; Fortin, D.; Hannington, M.D.; Schwarz-Schampera, U. Preliminary characterization and biological reduction of putative biogenic iron oxides (BIOS) from the Tonga-Kermadec Arc, Southwest Pacific Ocean. *Geobiology* **2009**, *7*, 35–49. [\[CrossRef\]](#)
61. Li, J.; Peng, X.; Zhou, H.; Li, J.; Sun, Z. Molecular evidence for microorganisms participating in Fe, Mn, and S biogeochemical cycling in two low-temperature hydrothermal fields at the Southwest Indian Ridge. *J. Geophys. Res. Biogeosci.* **2013**, *118*, 665–679. [\[CrossRef\]](#)
62. Roden, E.E. Fe(III) Oxide Reactivity Toward Biological versus Chemical Reduction. *Environ. Sci. Technol.* **2003**, *37*, 1319–1324. [\[CrossRef\]](#)
63. Hu, Y.; Feng, D.; Chen, L.; Zheng, G.; Peckmann, J.; Chen, D. Using iron speciation in authigenic carbonates from hydrocarbon seeps to trace variable redox conditions. *Mar. Petrol. Geol.* **2015**, *67*, 111–119. [\[CrossRef\]](#)
64. Pierre, C.; Blanc-Valleron, M.M.; Caqueneau, S.; März, C.; Ravelo, A.C.; Takahashi, K.; Zarikian, C.A. Mineralogical, geochemical and isotopic characterization of authigenic carbonates from the methane-bearing sediments of the Bering Sea continental margin (IODP Expedition 323, Sites U1343–U1345). *Deep Sea Res. Part II* **2016**, *125*, 133–144. [\[CrossRef\]](#)
65. Tong, H.; Feng, D.; Cheng, H.; Yang, S.; Wang, H.; Min, A.G.; Edwards, R.L.; Chen, Z.; Chen, D. Authigenic carbonates from seeps on the northern continental slope of the South China Sea: New insights into fluid sources and geochronology. *Mar. Petrol. Geol.* **2013**, *43*, 260–271. [\[CrossRef\]](#)
66. Matsumoto, R. Isotopically heavy oxygen containing siderite derived from the decomposition of methane hydrate. *Geology* **1989**, *17*, 707–710. [\[CrossRef\]](#)
67. Mozley, P.S.; Wersin, P. Isotopic composition of siderite as an indicator of depositional environment. *Geology* **1992**, *20*, 817–820. [\[CrossRef\]](#)

68. Pierre, C.; Bayon, G.; Blanc-Valleron, M.M.; Mascle, J.; Dupré, S. Authigenic carbonates related to active seepage of methane-rich hot brines at the Cheops mud volcano, Menes caldera (Nile deep-sea fan, eastern Mediterranean Sea). *Geo Mar. Lett.* **2014**, *34*, 253–267. [[CrossRef](#)]
69. Viola, I.; Capozzi, R.; Bernasconi, S.M.; Rickli, J. Carbon, oxygen and strontium isotopic constraints on fluid sources, temperatures and biogeochemical processes during the formation of seep carbonates–Secchia River site, Northern Apennines. *Sediment. Geol.* **2017**, *357*, 1–15. [[CrossRef](#)]
70. Achtnich, C.; Bak, F.; Conrad, R. Competition for electron donors among nitrate reducers, ferric iron reducers, sulfate reducers, and methanogens in anoxic paddy soil. *Biol. Fert. Soils.* **1995**, *19*, 65–72. [[CrossRef](#)]
71. Lovley, D.R.; Phillips, E.J. Competitive mechanisms for inhibition of sulfate reduction and methane production in the zone of ferric iron reduction in sediments. *Appl. Microbiol. Biotechnol.* **1987**, *53*, 2636–2641. [[CrossRef](#)]
72. Van Cappellen, P.; Wang, Y. Cycling of iron and manganese in surface sediments; a general theory for the coupled transport and reaction of carbon, oxygen, nitrogen, sulfur, iron, and manganese. *Am. J. Sci.* **1996**, *296*, 197–243. [[CrossRef](#)]
73. Hong, W.L.; Torres, M.E.; Kim, J.H.; Choi, J.; Bahk, J.J. Carbon cycling within the sulfate-methane-transition-zone in marine sediments from the Ulleung Basin. *Biogeochemistry* **2013**, *115*, 129–148. [[CrossRef](#)]
74. Chen, F.; Chen, J.; Jin, H.; Li, H. Correlation of $\delta^{13}\text{C}_{\text{org}}$ in surface sediments with sinking particulate matter in south china sea and implication for reconstructing paleo-environment. *Acta Sedimentol. Sin.* **2012**, *30*, 340–345, (In Chinese with English Abstract). [[CrossRef](#)]
75. Feng, J.; Yang, S.; Wang, H.; Liang, J.; Fang, Y.; Luo, M. Methane source and turnover in the shallow sediments to the west of Haima cold seeps on the northwestern slope of the South China Sea. *Geofluids* **2019**, *2019*, 1–18. [[CrossRef](#)]
76. Borowski, W.S.; Hoehler, T.M.; Alperin, M.J.; Rodriguez, N.M.; Paull, C.K. Significance of anaerobic methane oxidation in methane-rich sediments overlying the Blake Ridge gas hydrates. *NASA Ames Res. Cent.* **2000**, *164*, 87–99.
77. Li, Q.; Cai, F.; Liang, J.; Shao, H.; Dong, G.; Wang, F.; Yang, C.S.; Hu, G. Geochemical constraints on the methane seep activity in western slope of the middle Okinawa Trough, the East China Sea. *Sci. China Earth Sci.* **2015**, *58*, 986–995. [[CrossRef](#)]
78. Berner, R.A. *Early Diagenesis: A Theoretical Approach*, 1st ed.; Princeton University Press: Princeton, NJ, USA, 1980.
79. Xu, C.; Wu, N.; Sun, Z.; Zhang, X.; Geng, W.; Cao, H.; Wang, L.; Zhang, X.; Xu, G. Methane seepage inferred from pore water geochemistry in shallow sediments in the western slope of the Mid-Okinawa Trough. *Mar. Petrol. Geol.* **2018**, *98*, 306–315. [[CrossRef](#)]
80. Haeckel, M.; Boudreau, B.P.; Wallmann, K. Bubble-induced porewater mixing: A 3-D model for deep porewater irrigation. *Geochem. Cosmochim. Acta.* **2007**, *71*, 5135–5154. [[CrossRef](#)]
81. Wu, D.; Wu, N.; Ye, Y.; Zhang, M.; Liu, L.; Guan, H.; Cong, X. Early diagenesis records and pore water composition of methane-seep sediments from the southeast Hainan basin, South China Sea. *J. Geol. Res.* **2011**, *2011*, 1–10. [[CrossRef](#)]
82. Chen, F.; Su, X.; Nürnberg, D.; Lu, H.; Zhu, Y.; Liu, J.; Liao, Z. Lithologic features of sediments characterized by high sedimentation rates since the last glacial maximum from Dongsha area of the South China Sea. *Mar. Geol. Quart. Geol.* **2006**, *26*, 9–17, (In Chinese with English Abstract). [[CrossRef](#)]
83. He, Z.; Zhang, Q.; Feng, Y.; Luo, H.; Pan, X.; Gadd, G.M. Microbiological and environmental significance of metal-dependent anaerobic oxidation of methane. *Sci. Total Environ.* **2018**, *610*, 759–768. [[CrossRef](#)]
84. Li, W.; Alves, T.M.; Wu, S.; Rebesco, M.; Zhao, F.; Mi, L.; Ma, B. A giant, submarine creep zone as a precursor of large-scale slope instability offshore the Dongsha Islands (South China Sea). *Earth Planet. Sci. Lett.* **2016**, *451*, 272–284. [[CrossRef](#)]
85. Liu, J.; Zhu, R.; Liang, X.; Ma, L.; Lin, X.; Zhu, J.; He, H.; Parker, S.C.; Molinari, M. Synergistic adsorption of Cd(II) with sulfate/phosphate on ferrihydrite: An in situ ATR-FTIR/2D-COS study. *Chem. Geol.* **2018**, *477*, 12–21. [[CrossRef](#)]
86. Treude, N.; Rosencrantz, D.; Liesack, W.; Schnell, S. Strain FAc12, a dissimilatory iron-reducing member of the *Anaeromyxobacter* subgroup of *Myxococcales*. *FEMS Microbiol. Ecol.* **2003**, *44*, 261–269. [[CrossRef](#)]
87. Fu, L.; Li, S.W.; Ding, Z.W.; Ding, J.; Lu, Y.Z.; Zeng, R.J. Iron reduction in the DAMO/*Shewanella oneidensis* MR-1 coculture system and the fate of Fe(II). *Water Res.* **2016**, *88*, 808–815. [[CrossRef](#)] [[PubMed](#)]

88. Swedlund, P.J.; Webster, J.G. Adsorption and polymerisation of silicic acid on ferrihydrite, and its effect on arsenic adsorption. *Water Res.* **1999**, *33*, 3413–3422. [[CrossRef](#)]
89. Zachara, J.M.; Girvin, D.C.; Schmidt, R.L.; Resch, C.T. Chromate adsorption on amorphous iron oxyhydroxide in the presence of major groundwater ions. *Environ. Sci. Technol.* **1987**, *21*, 589–594. [[CrossRef](#)] [[PubMed](#)]
90. Golden, D.C. Ion Exchange, Thermal Transformations, and Oxidizing Properties of Birnessite. *Clay Clay Miner.* **1986**, *34*, 511–520. [[CrossRef](#)]
91. Mckenzie, R.M. The surface charge on manganese dioxides. *Soil Res.* **1981**, *19*, 41–50. [[CrossRef](#)]
92. González, F.J.; Somoza, L.; Lunar, R.; Martínez-Frías, J.; Rubí, J.M.; Torres, T.; Ortiz, J.E.; Díaz-del-Río, V. Internal features, mineralogy and geochemistry of ferromanganese nodules from the Gulf of Cadiz: The role of the Mediterranean outflow water undercurrent. *J. Mar. Syst.* **2010**, *80*, 203–218. [[CrossRef](#)]
93. Magalhães, V.H.; Pinheiro, L.M.; Ivanov, M.K.; Kozlova, E.; Blinova, V.; Kolganova, J.; Vasconcelos, C.; McKenzie, J.A.; Bernasconi, S.M.; Kopf, A.J. Formation processes of methane-derived authigenic carbonates from the Gulf of Cadiz. *Sediment. Geol.* **2012**, *243*, 155–168. [[CrossRef](#)]
94. Cangemi, M.; Di Leonardo, R.; Bellanca, A.; Cundy, A.; Neri, R.; Angelone, M. Geochemistry and mineralogy of sediments and authigenic carbonates from the Malta Plateau, Strait of Sicily (Central Mediterranean): Relationships with mud/fluid release from a mud volcano system. *Chem. Geol.* **2010**, *276*, 294–308. [[CrossRef](#)]
95. Zheng, G.; Fu, B.; Takahashi, Y.; Kuno, A.; Matsuo, M.; Zhang, J. Chemical speciation of redox sensitive elements during hydrocarbon leaching in the Junggar Basin, Northwest China. *J. Asian Earth Sci.* **2010**, *39*, 713–723. [[CrossRef](#)]
96. Yan, Z.; Joshi, P.; Gorski, C.A.; Ferry, J.G. A biochemical framework for anaerobic oxidation of methane driven by Fe(III)-dependent respiration. *Nat. Commun.* **2018**, *9*, 1642. [[CrossRef](#)] [[PubMed](#)]



© 2019 by the authors. Licensee MDPI, Basel, Switzerland. This article is an open access article distributed under the terms and conditions of the Creative Commons Attribution (CC BY) license (<http://creativecommons.org/licenses/by/4.0/>).